PERGAMON

Progress in Surface Science 67 (2001) 99–121

Progress in SURFACE SCIENCE

www.elsevier.com/locate/progsurf

Experiments on individual alumina-supported adatoms and clusters

N. Nilius, A. Cörper, G. Bozdech, N. Ernst *, H.-J. Freund

Fritz-Haber-Institut der Max-Planck-Gesellschaft, Abteilung Chemische Physik, Faradayweg 4-6, D-14195 Berlin, Germany

Abstract

To contribute to an understanding of growth conditions and electronic properties of metal clusters on technologically relevant oxides we have examined the mobility of individual, alumina-supported Pt-adatoms and the optical properties of single supported Ag-clusters. Using field-ion microscopy (FIM) we have prepared and imaged an individual Pt-adatom at approximately 40 K, both on the apex plane of a [1 1 0]-oriented NiAl tip and on a thin alumina film, grown on the same NiAl specimen by oxidation. On the alumina film, the onset temperature for Pt surface diffusion approaches 100 K being distinctively lower than the value 165 K measured on NiAl(1 1 0). Employing the tip of a scanning tunneling microscope (STM) as a local electron source, photon emission from individual, alumina-supported Ag-clusters was spectroscopically analyzed. The occurrence of a distinct emission line is explained by the decay of a collective electron oscillation (Mie-plasmon resonance). For decreasing Ag-cluster diameter, the emission lines (i) shift to higher energies and (ii) their widths increase. To explain these observations, we discuss (i) the reduced screening of the plasmon oscillation due to the Ag 4d electrons and (ii) an enhanced electron surface scattering rate in small clusters.

Keywords: Ordered oxide film; Metal deposition; Field-ion and field-electron emission microscopy; Scanning tunneling microscopy; Photon emission spectroscopy; Surface diffusion; Structure; Optical and electronic properties

1. Introduction

Thin oxide films, supporting small metal aggregates, are of great technological importance, since they act as model systems for heterogeneous catalysis [1–6].

* Corresponding author. Tel.: +49-30-8413-4180; fax: +49-30-8413-4306.
E-mail addresses: nilius@fhi-berlin.mpg.de (N. Nilius), ernst@fhi-berlin.mpg.de (N. Ernst).

0079-6816/01/$ - see front matter
PII: S0079-6816(01)00018-1

Following a relatively early report [7] on the structural characterization of an ordered aluminum oxide on NiAl(1 1 0), a series of investigations was carried out on this particular system, using the arsenal of modern surface science techniques including high resolution imaging methods, such as high resolution electron microscopy (HREM) and scanning tunneling microscopy (STM). Charging effects limit the application of most surface physics techniques to extremely thin films that can be produced in different ways. When the surface of a NiAl crystal is exposed to oxygen, the formation of an alumina film is thermodynamically favored at proper conditions. Structural and electronic properties of such aluminum oxide films have been established, especially for the close-packed NiAl(1 1 0) surface. In this case, a well-ordered thin aluminum oxide film ($\sim$0.5 nm) can be grown [2,6]. The various experimental results obtained suggest that the stoichiometry and structure of the oxide is compatible with γ-Al_2O_3. A schematic structure model of the oxide film is sketched in Fig. 1.

In the field-emission community, attempts preparing and characterizing metals on less ordered and relatively thick oxides, such as Ni/Rh_2O_3 [8] and $Pd–Mo/Al_2O_3/W$, have been reported [9]. Using atom-probe field-ion microscopy (AP-FIM) the oxidation of a Ni-rich NiAl alloy has been characterized. However, no ordering of the oxide film was reported [10]. We are not aware of any reports on FIM, HREM and STM observations of individual metal adatoms deposited on a well-ordered oxide. With the aim of contributing to the energetics and kinetics of the diffusion and clustering of individual metal adatoms on an ordered oxide film, we have applied FIM and field-electron microscopy (FEM) on the system Al_2O_3 on NiAl(1 1 0). Recently, we have prepared and characterized an ordered Al_2O_3 film on a [1 1 0]-oriented NiAl tip and showed the feasibility of FIM studies of an *ensemble* of Pt-adatoms deposited on the alumina film [11]. In Section 3.1, we present our most recent FIM observations on *individual* alumina-supported Pt-adatoms, using an improved probe-hole FIM–FEM technique.

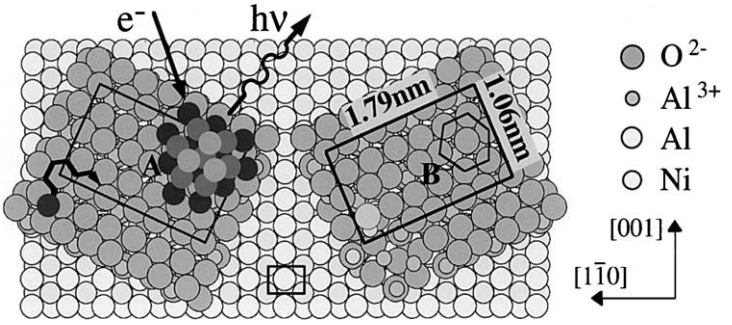

Fig. 1. Schematic structure models. Unit meshes of domains A and B of oxide film are shown. Rectangle in middle illustrates symmetry of NiAl(1 1 0) substrate surface and distorted hexagon indicates arrangement of oxygen ions in domain B of alumina film. Migration of individual adatom and electron-induced photon emission from small, oxide-supported cluster are also schematically sketched.

For the structural and electronic characterization of clusters, formed after vapor deposition of metal atoms, a *thin*, well-ordered oxide film is also the substrate of choice. The cluster–oxide interaction is influenced by the variation of the film composition, film morphology and substrate temperature [1–3,6], which opens up the possibility of adjusting the cluster density and the mean cluster size at the surface. The limited height of the oxide film and its transparency to low-energy electrons allow the application of the conventional methods of surface science. Additionally, the film acts as a spacer between the cluster and the underlying metal, and minimizes the coupling between the two electron reservoirs.

The investigation of metal nanoparticles at the surface is complicated by the limited lateral resolution of conventional electron and optical spectroscopies. Usually, these methods average over macroscopic areas of the sample surface; the experimental results are therefore obtained for an ensemble of objects and are inhomogeneously broadened by a number of statistical factors, e.g., size distribution of deposited particles and variations in the local environment. The structural and electronic properties of the individual objects under study are often hidden in the average obtained for the ensemble. Many attempts have been made to increase the spatial resolution of the spectroscopy and open the possibility of investigating single, selected structures on a nanometer scale. Most of these experiments are based on the high resolution abilities of STM and its variants. Tunneling spectroscopy allows the determination of the electronic structure of small metal clusters [4,12,13] and, recently, the observation of vibrational spectra of single adsorbed molecules [14]. Photon emission from the tunnel junction of an STM, stimulated by inelastic tunneling processes, can be used to measure the optical properties of the sample surface in the nanometer regime [15]. The method has been employed to record photon maps of semiconductors or metal films [16,17], nanocrystals [18,19] and individual molecules [20] as well. The spectroscopic mode allows the assignment of the observed photon emission to elementary processes, such as interface plasmons in the tip-sample cavity or interband transitions in the sample [16].

Due to their characteristic surface plasmon resonance, silver particles have always played a prominent role in absorption and emission spectroscopy [21]. The resonance position can be used to probe the size, shape and chemical environment of the clusters. A large basis of measurements is available for *ensembles* of silver particles, either supported on insulating surfaces (quartz [22], TiO_2 [23]), or embedded in weakly interacting matrices (glass [24], argon [25]). Various theoretical models have also been developed to help explain the experimental data [25–27]. In Section 3.2, we report on photon emission spectra of individual alumina-supported silver clusters, as a function of size. We present the energetic position of the plasmon resonances for cluster sizes between 1.5 and 12 nm diameter, as well as the widths of resonances for individual clusters [28]. A contribution is made to the optical spectroscopy of individual, nanosized particles, which are of great importance for different technological applications, including heterogeneous catalysis.

2. Experimental procedures

2.1. Field-ion microscopy

A thin oxide film has been prepared according to previously described procedures [6]. The NiAl tips, used as substrates for the oxidation process, were produced in four steps: (i) cutting of [1 1 0]-oriented rods from a single crystal, (ii) cleaning of the rods through heating in ultrahigh vacuum (UHV), (iii) electrolytic etching in air and finally (iv) preparation of the tip in an FIM set-up (Fig. 2) through heating cycles (to a maximum temperature of 1300 K), neon-ion sputtering and field evaporation (FEV). Pulsed FEV at $T \approx 35$ K was employed, which reduced the effect of preferential removal of aluminum ions [29] that deteriorate the formation of an alumina film during oxidation. For probe-hole FIM–FEM measurements, our recently improved UHV set-up (base pressure $P < 1 \times 10^{-11}$ mbar) allows field-ion and electron spectroscopy of selected surface sites. Energy analyses can be carried out in a hemispherical mirror analyzer [30], which was especially useful for measurements of the low-energy side of electron energy distributions. From energy distribution and

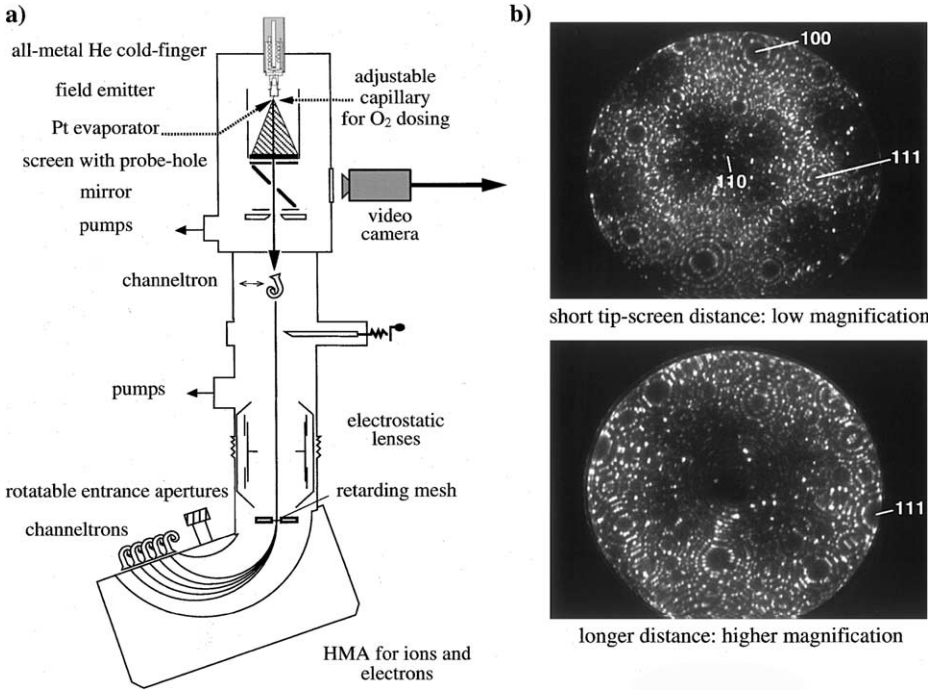

Fig. 2. Experimental set-up and FIM of [1 1 0]-NiAl: (a) Specimens are oxidized in situ using an adjustable capillary for O_2 dosing. Hole in channel plate-screen arrangement allows spectroscopic measurements of ions and electrons field emitted from the apex of tip. (b) NiAl specimen was flash heated to approximately 1000 K followed by pulsed FEV at 35 K. To improve characterization of (1 1 0) apex region, He cold-finger, supporting tip, can be manipulated such that tip-screen distance (magnification) increases.

Table 1
Work-function data of clean NiAl(1 1 0)

Pretreatment	Work function (eV)	Al surface concentration
dc FEV, 79 K	5.6	Low
Flash, 1300 K	5.1	High

I–V, Fowler–Nordheim (FN) measurements, work function data of NiAl (1 1 0) were determined and are listed in Table 1 [11]. These measurements helped to improve the surface conditions prior to oxidation.

2.2. Photon emission spectroscopy combined with STM

Experiments have been performed in two UHV chambers connected by a UHV-transfer rod facility for in situ sample preparation and STM analysis (base pressure $P < 2 \times 10^{-10}$ mbar). To maximize the acceptance angle for the photon detection a beetle-type STM with its open construction has been used (Fig. 3). The STM is completely surrounded by a parabolic mirror, whereby the tip-sample region is adjusted in the focal point. Outside the vacuum chamber, the light is focused on the entrance slit of a grating spectrograph and detected with a liquid nitrogen cooled, charge coupled device (CCD) camera. The accessible energy range for photon detection is between 1 and 6 eV and is restricted by the performance of the CCD-chip. The preparation chamber is equipped with standard UHV-facilities for sample preparation and analysis, including an ion-gun and a low-energy electron diffraction (LEED) system. The tunnel tips were electrochemically etched from a polycrystalline tungsten wire.

In the experiment, field-emitted electrons from the tunnel tip are injected into the sample surface (Fig. 3(a)). The electron energies are typically adjusted to 10 V and the electron current is below 10 nA. As in FIM experiments, an ultrathin alumina film is used as substrate. The film is grown on the (1 1 0) surface of a NiAl single crystal by oxidation and annealing steps to 1300 K. The film shows a perfect long range order, reflected in a characteristic, sharp LEED-pattern. Silver was evaporated from a crucible by electron bombardment and deposited onto the alumina film at 300 K. A detailed description of the preparation procedure can be found elsewhere [6,31].

Because of the weak metal/oxide interaction, silver grows at 300 K in the Volmer–Weber mode, forming three-dimensional particles [6]. Step edges and domain boundaries of the alumina film are the preferential nucleation centers, leading to a low nucleation density and rather large particle sizes (see Section 3.2, Fig. 9(a), upper image). The high mobility of the Ag-clusters gives rise to modifications of the sample morphology, induced by the scanning process of the STM tip. To increase the stability of the deposited material, the sample was held at negative potential with respect to the evaporator during the deposition process (−500 V). A small fraction of silver atoms, leaving the crucible in an ionized state (Ag^+), is accelerated to the surface and causes the formation of additional nucleation centers. This preparation procedure leads to an almost-isotropic nucleation density at the surface and a narrower size distribution of the silver particles (Section 3.2, Fig. 9(a), lower image). As a function of evaporated material, the mean cluster size can be adjusted to between

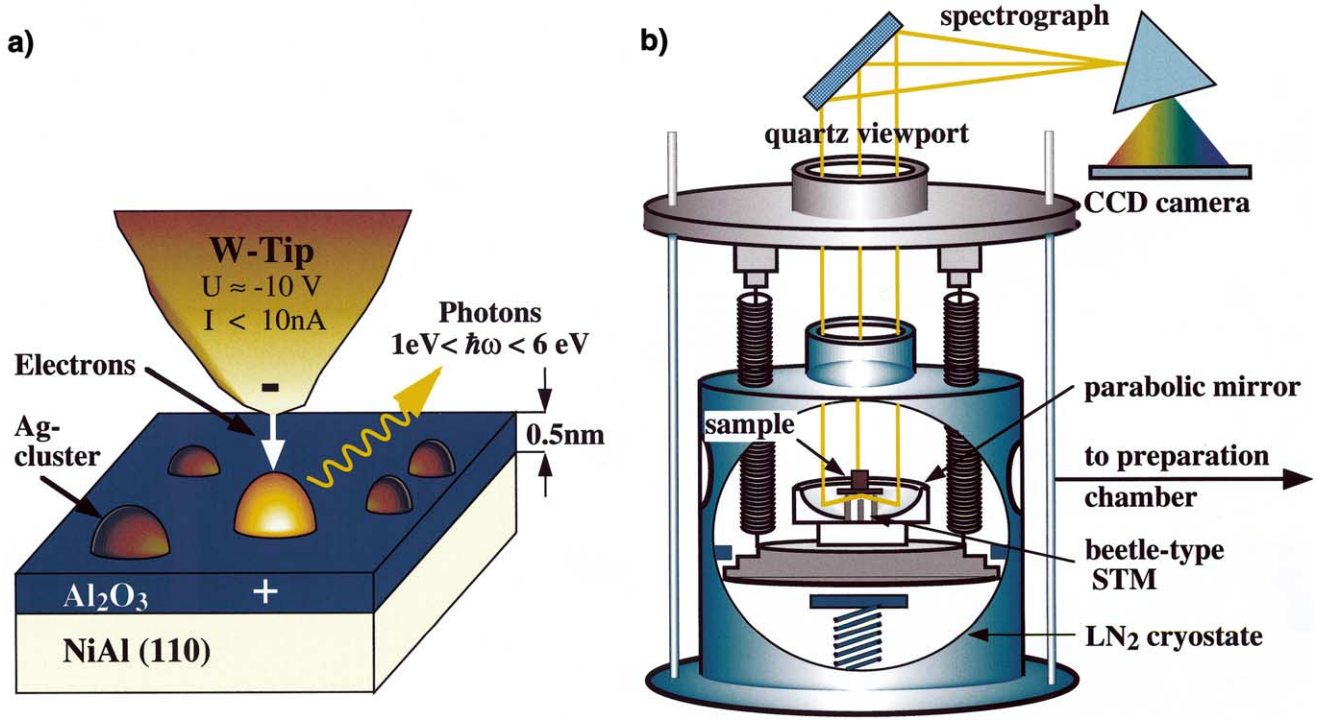

Fig. 3. Photon emission spectroscopy of single silver clusters supported on thin alumina film (0.5 nm) in STM. (a) Schematic drawing illustrates cavity below W tunnel tip. Electrons with given parameters (tunnel voltage, current) are injected from tip into individual Ag-particles, subsequently emitted photons are detected in energy range between 1 and 6 eV. (b) Analysis part of experimental set-up consists of beetle-type STM (tip direction upwards), housed in UHV chamber combined with grating spectrograph and CCD camera in air. Sample is prepared and characterized in second chamber and can be moved using transfer rod in UHV.

1 and 12 nm at a nearly constant cluster density of $4 \times 10^{12}/\mathrm{cm}^2$. An STM image of the sample region was taken before and after each spectroscopic run to exclude morphological changes of the surface. Cluster diameters were determined after separating the effect of tip convolution, which was achieved by estimating the mean tip radius from the apparent broadening of substrate step edges. However, the given sizes still have to be taken as an upper limit of the real cluster diameter, because the exact tip radius is not known.

3. Results and discussion

3.1. Mobility of individual platinum adatoms

3.1.1. Platinum on NiAl(1 1 0)

FIM-observations on platinum adatoms deposited on NiAl(1 1 0) were primarily carried out to (i) optimize the position of the tip relative to the beam of platinum atoms from the evaporator and (ii) to produce a map of binding sites used to calibrate the local magnification before oxidizing the [1 1 0]-oriented NiAl tip. From earlier observations on single adatom diffusion, it is known that the magnification decreases from edge to center by a factor of almost two, especially if one prepares larger planes [32,33]. Since the atomic structure of the NiAl(1 1 0) substrate is well established, our approach intends to make displacement observations on the oxide film, grown on the same NiAl(1 1 0) plane, more reliable. Fig. 4 shows the result using neon FIM at 35 K. In this case, a Pt-adatom was placed almost in the center of a NiAl(1 1 0) apex plane shaped by FEV at 35 K. Several heating cycles at 150 K did *not* lead to an observable displacement. However, a small displacement was observed after the ninth heating step at 165 K (20 s). By comparing the direction of the adatom motion with the lattice of the substrate atoms, as in Fig. 4(d), an estimate of the displacement distance is made possible. The orientation of the NiAl(1 1 0) unit cell was obtained from an FIM observation of the positions of (1 0 0) and (1 1 1) facets (visualized, e.g., in Fig. 2(b)), which allowed the zone lines and spatial directions for an ordered sample to be assigned with high accuracy, and gave 0.87 nm for the actual displacement distance. Together with the observations made at 150 K, we conclude that the onset for surface diffusion is close to 165 K.

Assuming a two-dimensional random walk for the adatom migration, one may estimate the activation energy barrier, E_d, by using the relation [34], viz.,

$$E_\mathrm{d} = -kT \ln(\langle r^2 \rangle / 4 D_0 \tau), \tag{3.1}$$

where k is Boltzmann's constant, T the surface temperature, $\langle r^2 \rangle$ the mean square displacement, τ the diffusion-time interval. The prefactor D_0 was calculated from

$$D_0 \approx 0.25 l^2 kT/h, \tag{3.2}$$

h being Planck's constant. The elementary diffusion length, l, was assumed to be 0.25 nm, as suggested by the surface structure of NiAl(1 1 0), shown in Fig. 4(d). Setting $\langle r^2 \rangle \approx 0.01$ nm^2, one gets E_d(Pt/NiAl(1 1 0)) ≈ 0.48 eV with an accuracy of approx-

imately 10% [34]. To our knowledge, no experimental and calculated activation energies have been previously reported for Pt/NiAl(1 1 0), but we note that our E_d value of 0.48 eV is at least a factor of two *larger* than reported for Pt/Ni(1 1 1) (<0.22 eV) [34]. The surface diffusion behavior on the most densely packed, binary alloy surface NiAl(1 1 0) could, however be more involved since it is conceivable that the surface diffusion barrier heights depend on the Pt binding site (Ni or Al vicinity), as sketched in Fig. 4(d). The analysis of experimental displacements could become more complicated, as already noted for cluster diffusion [35] and for the diffusion behavior on heterogeneous surfaces characterized by Monte Carlo simulations [36].

3.1.2. Oxidation of a [1 1 0]-NiAl tip

To convey an impression of the results of the preparation procedures, we present observations of the clean and oxidized NiAl tip. FIM–FEM images, shown in Fig. 5, were obtained at T(NiAl) ≈ 35 K, allowing neon FIM under good resolution and contrast conditions. Pulsed FEV was employed for cleaning the specimen surface,

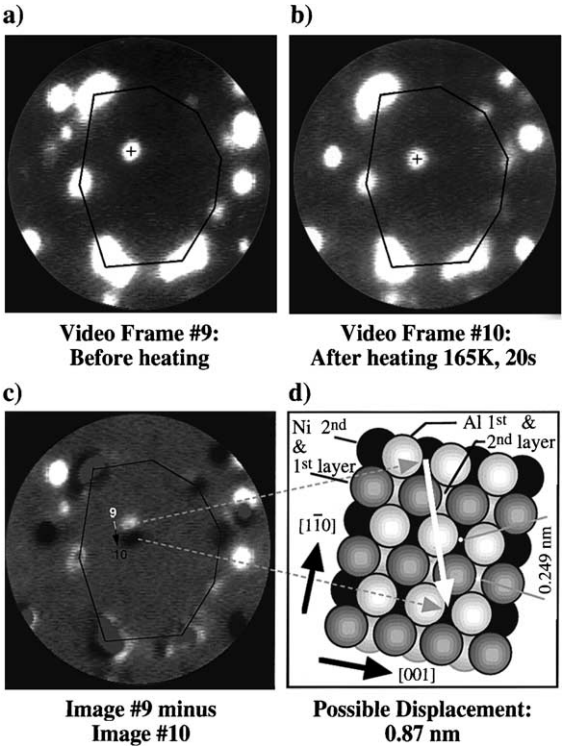

Fig. 4. Surface diffusion of Pt/NiAl(1 1 0). (a) Digitized video frame shows circular section of neon FIM image of Pt-adatom prepared on NiAl(1 1 0) plane shaped by low-temperature FEV. Boundary of NiAl(1 1 0) plane was marked by polygon curve, position of adatom by cross hair; (b) after heating for 20 s at 165 K, without applied field, the adatom has slightly moved. (c) This image shows result of subtracting (b) from (a). (d) Model illustrates displacement (0.87 nm) adatom has possibly experienced.

using a pulse to dc fraction of more than 20%, in order to minimize the effect of preferential FEV of aluminum ions [29]. One can also restore the surface concentration of Al by flashes to approximately 1000 K, as was mentioned in Section 2.1, by referring to Fig. 2(b). Our observations show that flashing to this temperature does not blunt the tip. We have routinely used this technique to approach the thermal end form [11]. Fig. 5(b) shows the shape of a thermally prepared tip characterized by an enlarged (1 1 0) plane. Compared to a low temperature FEV shape, a thermally

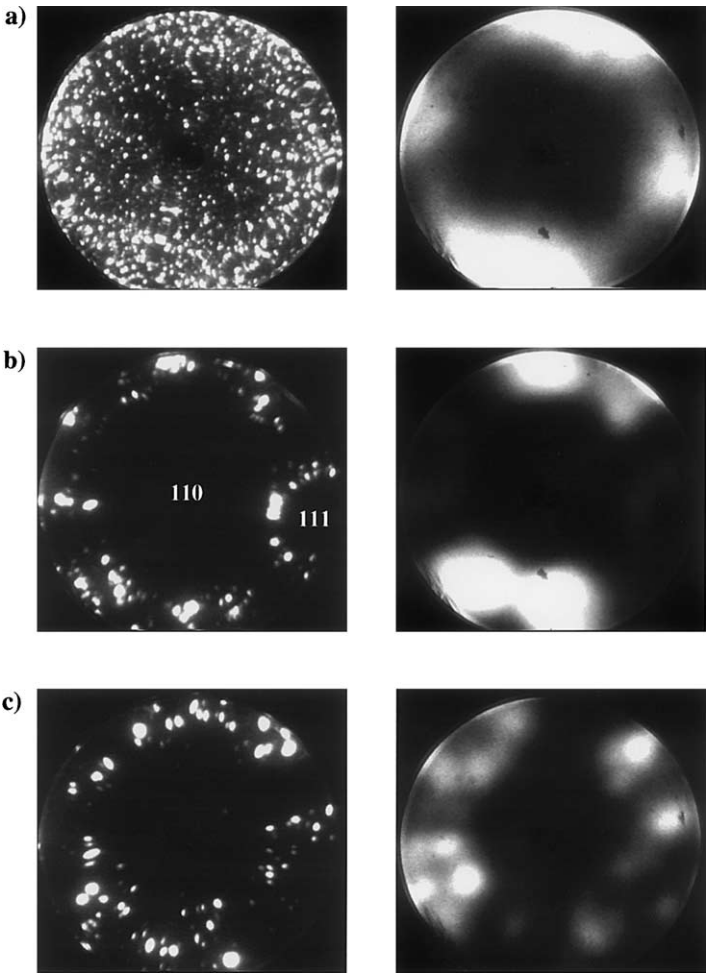

Fig. 5. On oxidation procedure of [1 1 0]-oriented NiAl(1 1 0) tip: in left and right columns, FIM and FEM images are shown; feature in center is probe hole. At approximately 6 o'clock, defect in sreen is visible, especially in FEM images. (a) To clean surface, pulsed FEV at 35 K was employed (dc-FEV: +14.15 kV, FEM-bias voltages: −850 V); (b) after flashing tip to 1000 K, (1 1 0)-facet size has increased (dc-FEV 9.0 kV). Then tip was dosed with oxygen at 67 K followed by exposure to 1500 Langmuir at 550 K. (c) After several temper cycles at 900 K, FE-current from (1 1 0) plane stayed constant (dc-FEV of alumina film 8.6 kV).

enlarged NiAl(1 1 0) facet can, of course, be covered by a larger number of Al_2O_3 unit cells.

The oxide film was formed following a procedure which included dissociative O_2 adsorption and flash heating to temperatures ranging between 700 and 1000 K [6,31]. In the example shown in Fig. 5(c), the tip was initially dosed with oxygen at 67 K to produce a chemisorbed O-layer. The adsorption of oxygen was monitored via the electron emission current, field emitted from the center of the (1 1 0) plane in Fig. 5(b). During this procedure, we made use of our probe-hole technique, including single electron counting (see Fig. 2(a)). The temporal dependence of this emission current is shown in Fig. 6. The change of the work function, $\Delta\Phi_{110}$, was calculated from the ratio of the emission current averaged over the time interval, $\Delta\tau$, and the current at time, t, $\langle I(\Delta\tau)\rangle/I(t)$, using the following relation, based on the FN equation, i.e.,

$$\Delta\Phi_{110}(t) = \left\{A^{-1}\ln\left(\langle I(\Delta\tau)\rangle/I(t)\right) + \{\Phi_{110}(\Delta\tau)\}^{3/2}\right\}^{2/3} - \Phi_{110}(\Delta\tau). \tag{3.3}$$

In this approach, we make use of the experimental condition that the temporal behavior of the field-electron emission current is dominated by the exponential expression of the FN equation, giving

$$I(t) \propto \exp\left(-A\{\Phi_{110}(t)\}^{3/2}\right). \tag{3.4}$$

To determine a value for $\langle I(\Delta\tau)\rangle$ one averages the electron emission current, e.g., between $\Delta\tau$ =300 and 360 s in Fig. 6. Since a value for the work function of clean

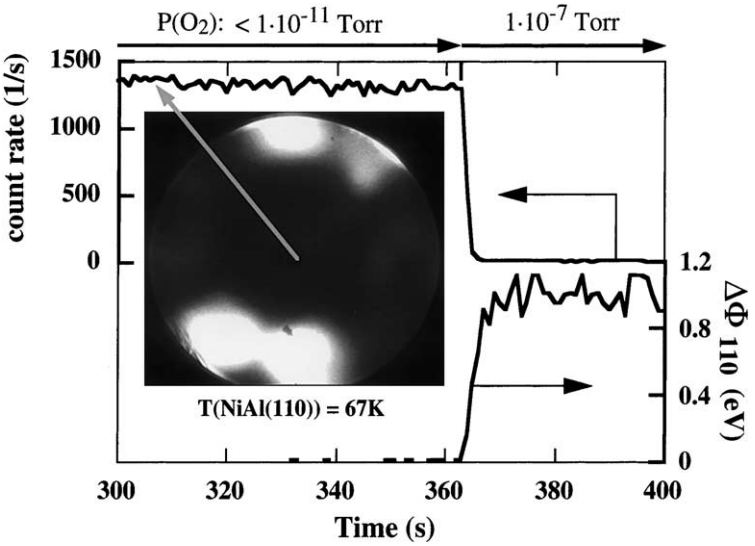

Fig. 6. Oxygen adsorption at 67 K on NiAl(1 1 0). FE-emission rate (upper curve, left scale) from center of top-most (1 1 0) surface (center of FEM pattern in inset) was measured as function of time. At 363 s O_2 pressure was raised to 1×10^{-7} Torr ($= 1.33 \times 10^{-7}$ mbar). Work-function change (lower curve, right scale) has been calculated from FE-emission rate and reaches maximum of 1 eV after 10 s.

NiAl(1 1 0) was derived from I–V and energy-distribution measurements [11] (Table 1), we introduce the following data in (3.3)

$$A = 1.8\ \mathrm{eV}^{-3/2} \quad \text{and} \quad \Phi_{110}(\Delta\tau) = 5.1\ \mathrm{eV}. \tag{3.5}$$

To summarize, the oxide film was prepared in three steps:

(i) *Oxygen adsorption*: After pulsed FEV at 35 K and flashing to 1000 K, the clean tip was dosed with oxygen at 67 K to produce a chemisorbed oxygen layer.

(ii) *Oxidation*: The tip was exposed to 1500 Langmuir oxygen at 550 K (field off).

(iii) *Ordering of the oxide film*: The tip was repeatedly tempered at approximately 900 K. Between the heating cycles, the FE current from the (1 1 0) plane was controlled. Tempering was finished when this current remained at a constant level.

After oxidation, FIM observations during FEV revealed that the oxide film covering the (1 1 0) facet, e.g., in Fig. 5(c), was approximately two layers thick. It was stable in the high-field conditions needed for low temperature (<79 K) neon FIM. It could be 'peeled off' from the surface in a controlled manner through FEV. The layer on the NiAl(1 1 0) apex plane came off at the end and showed the greatest stability. The oxide showed some amount of order, as deduced from FIM and FEM observations, but point defects could occasionally be discerned. Compared with the surface covered by chemisorbed oxygen, the NiAl(1 1 0), covered by an ordered alumina film, was more transparent to field-emitted electrons. Energy spectra showed onsets at the Fermi level, which were identical (within 30 meV) for the clean NiAl(1 1 0) and the oxidized surface [11], in agreement with the result of an earlier measurement for a Mo–tip coated with a thin alumina film [37].

3.1.3. Platinum on Al_2O_3/NiAl(1 1 0)

The feasibility to image platinum adatoms, supported on a thin alumina film, has recently been demonstrated in our group, using neon FIM at 79 K. At this temperature, the best image voltage (BIV) was not applied, since the oxide film, supporting the Pt-adatoms started to field desorb, albeit, slowly. At these conditions, neon FIM was characterized by strong fluctuations and non-optimum contrast. These drawbacks were partly compensated by computer aided superposition of selected video frames, which enabled weak features in the images stemming possibly from point defects on an otherwise perfect surface, to be visualized. Intending to observe cluster formation, the oxide surface was exposed to a relative high platinum dose, followed by several heating cycles (200–230 K, 10 s). As a result, a local ordering of Pt-adatoms was obtained in the vicinity of a point defect; the arrangement of adatoms was compatible with domain B of the Al_2O_3 unit cell [11]. From analyses of the adatom-ensemble displacements, a rough estimation of the diffusion activation-energy was possible, but it was concluded that more experiments should be carried out employing neon FIM below 50 K.

We have recently prepared an individual Pt-adatom on the apex plane of an oxidized [1 1 0]-oriented NiAl tip, using neon FIM at 35 K [38]. These observations were made in our improved probe-hole FIM set-up described in Section 2.1. A sequence of FIM patterns, obtained in an exploratory experiment, is shown in Fig. 7. The same specimen was also displayed in Fig. 5. The diameter of the top-most Al_2O_3

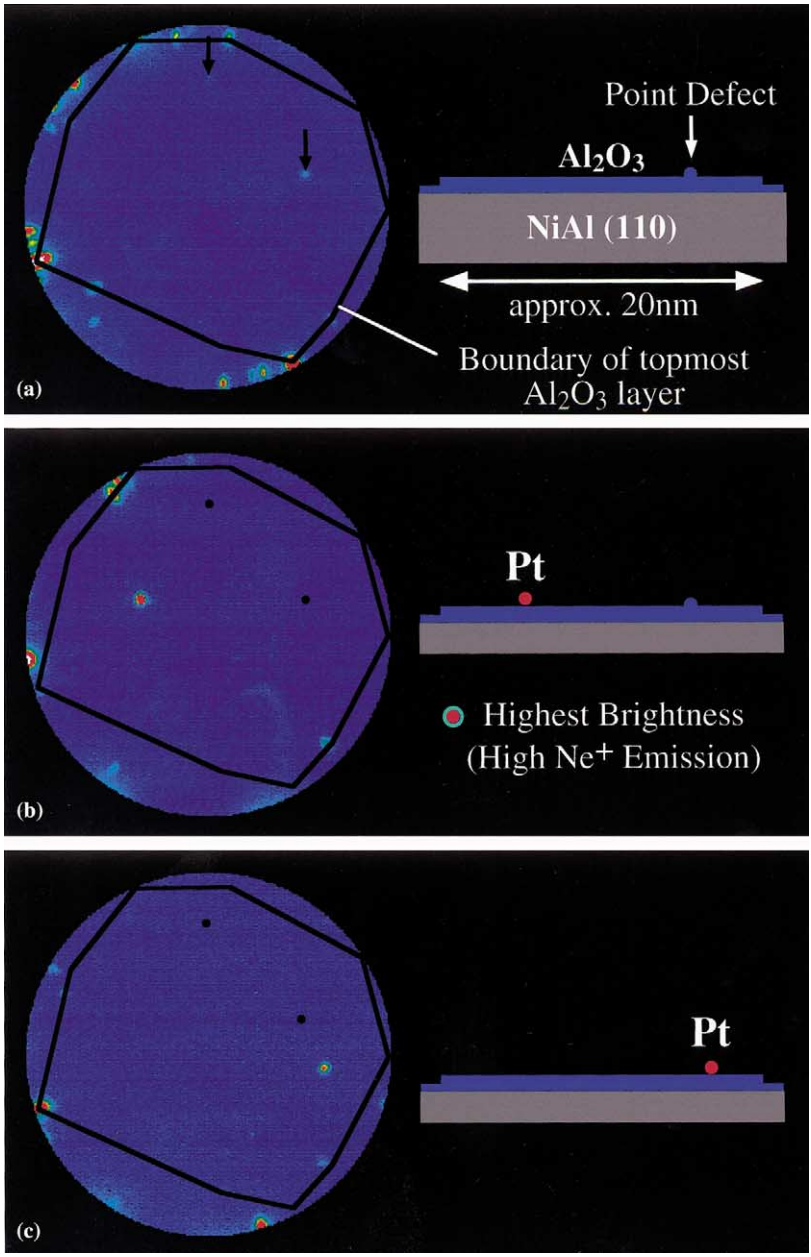

Fig. 7. Surface diffusion of $Pt/Al_2O_3/NiAl(1\,1\,0)$. Polygon curves have been drawn in circular sections of FIM-pattern to indicate boundary of top-most Al_2O_3 layer: (a) before Pt deposition. (b) After deposition, individual Pt-adatom was imaged at 35 K using neon FIM at 7.7 kV ($FEV(Al_2O_3) \approx 8.6$ kV, FEV (NiAl) ≈ 9.0 kV) (black dots: positions of defects). (c) After heating surface to 170 K during 20 s at zero field.

layer was estimated to be approximately 20 nm. This value was based on local radii determinations [39] employing ring counting between (1 1 0) apex and neighboring planes, such as (1 1 1) from FIM pattern in Fig. 5(a) and including the facetting of the tip apex upon heating [38]. Before deposition of platinum, the top-most Al_2O_3 film was imaged (using neon FIM at 35 K), so that sites at the boundary and possible point defects could be visualized, as in Fig. 7(a). The circular sections of FIM images in Fig. 7 show the specimen surface, after preparation procedures produced images displayed in Fig. 5 (FEV(NiAl) $\approx$ 9.0 kV, FEV(Al_2O_3) $\approx$ 8.6 kV at 35 K). After exposing the surface to a Pt-beam at 35 K, a new emission site at approximately 9 o'clock appeared, which has to be interpreted as the image spot of a single Pt-adatom. We note that the platinum exposure was increased by more than a factor of 10 to reach a Pt coverage on the alumina film comparable with Pt coverages on the top-most NiAl(1 1 0) layer. This indicates an apparently low sticking probability and/or accommodation of incoming Pt hitting the Al_2O_3 film (on the top-most NiAl(1 1 0) layer), which is in line with our earlier observations [11].

At this stage, we would like to discuss the imaging of the Pt-adatom which appears very bright and stable in Fig. 7(b). In this case, we applied a maximum voltage, 7.7 kV relative to a FEV voltage of approximately 8.6 kV for Al_2O_3/NiAl(1 1 0) and 9.0 kV for NiAl(1 1 0) at 35 K. Thus, for the conditions shown in Fig. 7(b) the field desorption voltage for a Pt-adatom on Al_2O_3/NiAl(1 1 0) is higher than 7.7 kV. The external field, several tens of a nanometer above the adatom, is estimated to 32 V/nm (3.2 V/Å) based on best image field conditions in Ne. However the local field strength in close vicinity above the Pt-adatom is conceivably higher [40]. Recently, calculations based on the density functional theory (DFT) at the local density approximation (LDA) level were carried out for Pt/Al_2O_3/Al(1 1 1) [41]. The results suggest ionic bonding of single Pt-atoms to the oxide film involving a significant electron-charge transfer from Pt to the substrate, even without an external field. This in turn might contribute to a further enhancement of the local field and field gradient, thus possibly increasing the local field-ionization current. A detailed understanding of the image formation mechanisms is certainly more involved. We conclude, that experimental conditions, such as imaging quality and resistance against field desorption, have in general been improved by cooling the tip from 79 to 35 K. Nevertheless, one has to take care to *not* field desorb the Pt-adatom, during imaging at 35 K, especially at sites close to the edge of a plane, where the electric field strength is higher than in the center.

Referring to Figs. 7(b) and (c), we note that the Pt-adatom leaves its site, as the surface is heated to 170 K for 20 s (field off). A new emission spot appeared at approximately 4 o'clock, almost 12 nm away from the initial site. To explain this observation two possibilities are considered: (i) the adatom diffuses from the site imaged in Fig. 7(b) (adatom (b)) to the site in Fig. 7(c) (adatom (c)) without leaving the top-most plane or, alternatively, (ii) adatom (b) migrates across the boundary *to* the periphery and another (or even the same) jumps *from* the periphery onto the top-most plane, finally ending up at the position in (c). At present, we do not know if the boundary is reflective for the given circumstances; we can therefore not discriminate between the two alternatives. We could, however, speculate that the atom is strongly

bound at a defect or step site, after passing the boundary and immobile thereafter, as discussed for metal on metal diffusion [42]. As a consequence, alternative (i) would possibly apply.

Fig. 8 shows the results of exploratory examinations of the surface diffusion behavior for alumina-supported, individual Pt-adatoms carried out on two different specimens. The upper diagram is based on cross hair analyses of FIM patterns, such as in Figs. 7(b) and (c) (image numbers 1 and 2). The lower set of data was deduced from observations on an individual Pt-adatom deposited in the center of the oxide plane [38]. The data in Fig. 8(a) clearly demonstrate that at 160 K the Pt-adatom is much more mobile on the oxide film than on NiAl(1 1 0), discussed in Section 3.1.1. During this experimental run, we could not reliably determine the onset temperature for surface diffusion on the alumina film. In the second experimental attempt (Fig. 8(b)), a quantification was possible; the identity of the adatom, located in the center of the plane was ascertained before and after the diffusion steps. In particular, upon the first heating step to 100 K for 15 s, the adatom changed its position slightly, but noticeably. In this case, our analysis of the jump direction is compatible with an hexagonal arrangement of lattice sites of domain B in Fig. 1 [38].

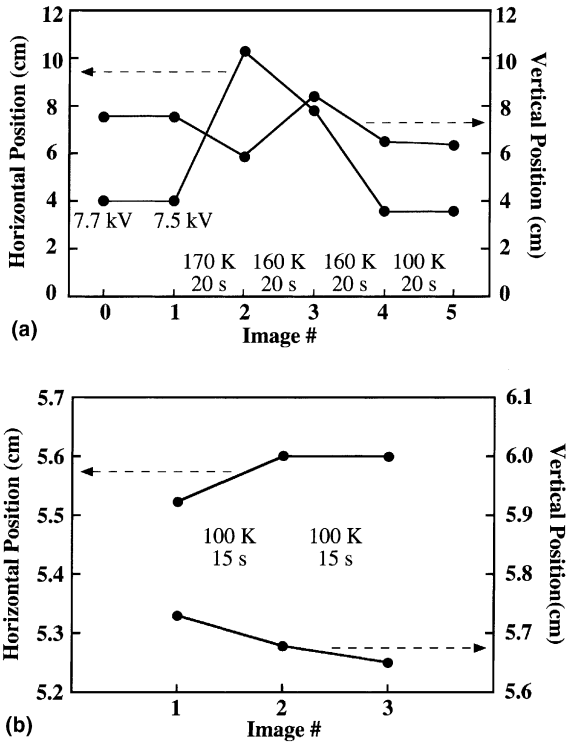

Fig. 8. Positions of image spots of Pt-adatoms diffusing on Al_2O_3/NiAl(1 1 0): (a) Between image cycles temperature was varied between 170 and 100 K (see Fig. 7). (b) Observations on adatom, prepared in the center of an oxide plane, suggest an onset temperature close to 100 K.

Table 2
Surface diffusion parameter for individual Pt-adatoms

System	Onset temperature (K)	Activation energy (eV)
Pt/NiAl(1 1 0)	165	0.48
Pt/Ni(1 1 1)		<0.22 [34]
$Pt/Al_2O_3/NiAl(1\,1\,0)$	>100	>0.29
	<160	<0.47
$Pt/Al_2O_3/Al(1\,1\,1)$		0.7 [41]

A summary of experimental and theoretical results of surface diffusion parameter for individual Pt-adatoms is given in Table 2. In our experiments carried out to date, those adatoms deposited on a thin alumina film supported by NiAl(1 1 0) showed an onset for surface diffusion, which is certainly well below 160 K and approaches 100 K. From these data, lower and upper limits of the diffusion activation energy (0.29–0.47 eV) were derived by applying (3.1). We note that our experimental estimate is significantly smaller than the recent theoretical result (0.7 eV) obtained for $Pt/Al_2O_3/Al(1\,1\,1)$ [41]. Though further experiments are still required, we conclude that the activation energy of Pt on a defect free area of Al_2O_3 is almost comparable with results of Pt surface diffusion on close-packed metal surfaces, such as Ni(1 1 1) and Pt(1 1 1) [34].

3.2. Photon emission spectroscopy of $Ag/Al_2O_3/NiAl(1\,1\,0)$

3.2.1. Emission from clean oxide and supported particles

The photon emission spectra of a clean alumina film on NiAl(1 1 0) are governed by two resonances of a tip induced plasmon excited in the NiAl/W tunnel junction (Fig. 9, curve (i)) [43]. This interface plasmon is the result of a strong electromagnetic interaction between the tip and the sample, causing collective electronic oscillations in the coupled electron gases (Fig. 10(a)) [44]. The thin insulating oxide film covering the NiAl-substrate does not change the shape of the emission spectrum. The total intensity of the emitted light decreases as the tunnel voltage increases, which reflects the retraction of the tunnel tip at higher voltages and the subsequent reduction of the electromagnetic coupling between tip and sample. At a tip bias above 10 V, the emission caused by the decay of tip induced plasmons almost vanishes.

In contrast, spectra taken on top of an Ag-cluster exhibit an intense emission line, centered around 3.7 eV (Fig. 9, curve (ii)). The additional peak appearing in the spectra at exactly half of the energy (1.85 eV) is the second-order diffraction peak of the spectrometer. The emitted intensity still increases for a tip bias above 10 V. The emission is polarity dependent, visible only for electron injection into the cluster (Fig. 9, curve (iii)). This behavior cannot be understood by using the concept of a radiating decay of the Ag/W interface plasmon, which is polarity independent by definition. Comparing the energetic position of the observed line with published experimental data allows an assignment of the emission to Mie-resonances inside the Ag-cluster (Fig. 10(b)) [21]. These resonances can be interpreted as collective

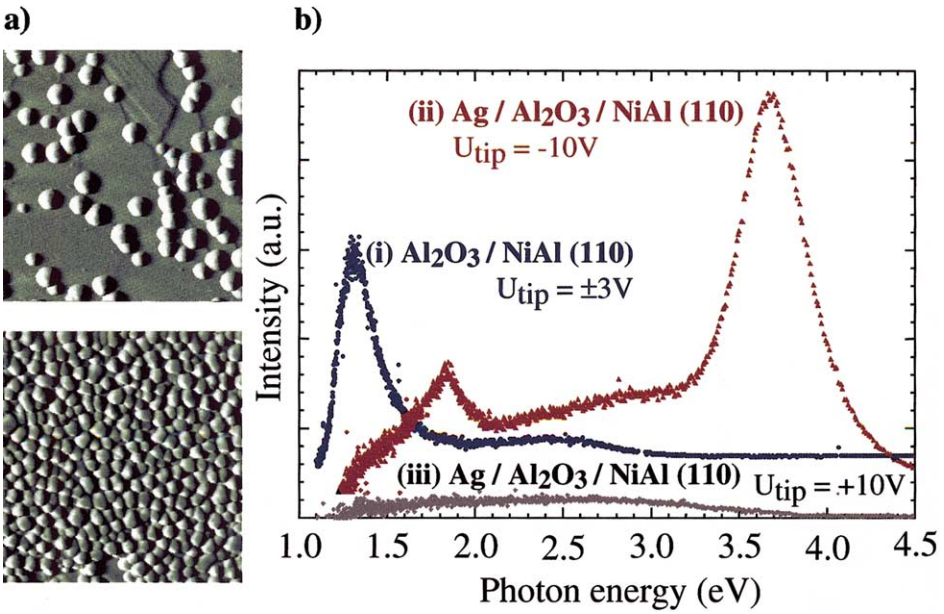

Fig. 9. Topography and emission spectra of $Ag/Al_2O_3/NiAl(110)$: (a) STM images of Ag-clusters on $Al_2O_3/NiAl(110)$ grown by vapor deposition (image sizes: 130 nm × 130 nm, $U_{tip} = -2$ V, $I_{gap} = 0.6$ nA). Sample was held at 0 V (upper left image) and −500 V (image below) relative to evaporator during Ag deposition. Only in latter case, clusters were stable enough to be analyzed. (b) Photon emission spectra were measured at three conditions (i) on clean alumina film and on Ag-clusters at (ii) negative and (iii) positive tip bias.

oscillations of the electron gas with respect to the Ag-ion cores driven by an external electromagnetic field (UV-radiation or electron injection). For non-spherical, supported metal clusters, the Mie-resonance divides into two modes, corresponding to an electron oscillation parallel (1,1-mode) and perpendicular to the substrate surface (1,0-mode) [21]. For geometrical reasons, only the perpendicular mode can be expected to show up in the present experimental data. On the one hand, electron injection from the tunnel tip follows the surface normal and preferentially leads to a dipole excitation perpendicular to the surface. On the other hand, the decay of Mie-resonances excited in plane, for instance due to electron-impact excitations, gives rise to a photon emission oriented along the tip-sample axis. This light will be absorbed or reflected at the tunnel tip and cannot reach the parabolic mirror directly. Therefore, the single emission line visible in the spectra has to be attributed to the decay of the (1,0) Mie-resonance in the Ag-cluster. The lateral resolution of the photon emission spectroscopy is determined by the diameter of the exciting electron beam. For a tunnel voltage of 10 V and a tunnel current of 10 nA, used in the experiments, the mean tip-sample separation is estimated as 1.0–1.5 nm, depending on the actual tip radius. The excitation of optical processes is therefore restricted to a sample area smaller than 1.5 nm in diameter. The observed photon emission has thus

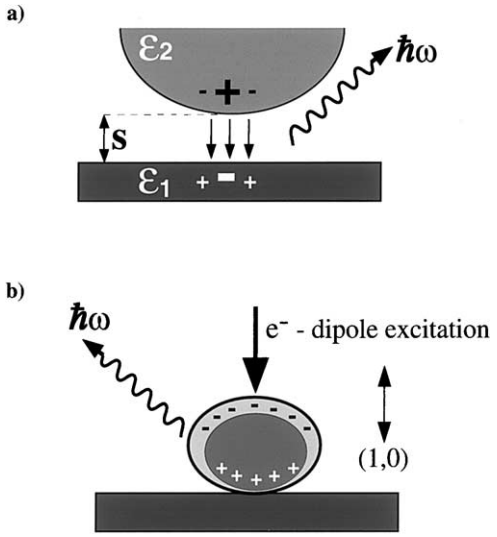

Fig. 10. Cross-sectional views illustrating possible photon emission events caused by excitation and decay of tip induced (a) and Mie (b) plasmons. In (a) dielectric properties of tip and sample govern emission processes; in (b) intrinsic optical properties of supported clusters are accessible through spectral analyses of emitted photons.

to be assigned to an individual Ag-cluster, the measured peak position, full-width-at-half-maximum (FWHM) and intensity of the emission line can be evaluated as a function of size and shape of a single cluster (Fig. 11).

3.2.2. Line width of Mie-plasmon

The low total photon yield emitted from an individual Ag-cluster complicates the evaluation of the FWHM of the Mie-resonance. The line widths measured in Fig. 11 result from a compromise between a reasonable signal-to-noise ratio and an optimal spectral resolution determined by the size of the entrance slit of the spectrograph. For the experimental data shown, a slit width of 1 mm was used and the intrinsic line-width of the resonance is additionally broadened by the transfer function of the spectrograph. For a slit width below 0.2 mm, the experimental broadening of the emission line is negligible but the required accumulation time for a single spectrum has to be extended, which increases the demands for thermal and structural stability of the tip-sample system. The general trend of the size dependence of the intrinsic line-broadening is presented in Fig. 12(a) (slit width 0.2 mm). Due to an enhanced surface scattering of the electron oscillation, followed by a dephasing of the collective mode, the line-width increases for smaller particle sizes. The measured broadening changes between 150 meV for cluster sizes above 8.0 nm and 300 meV for a cluster of approximately 2.0 nm. We note that a minimum line-width of 230 meV has previously been obtained for an ensemble of quartz-supported silver clusters with 10.0 nm mean cluster diameter and a narrow size distribution [45]. This difference to

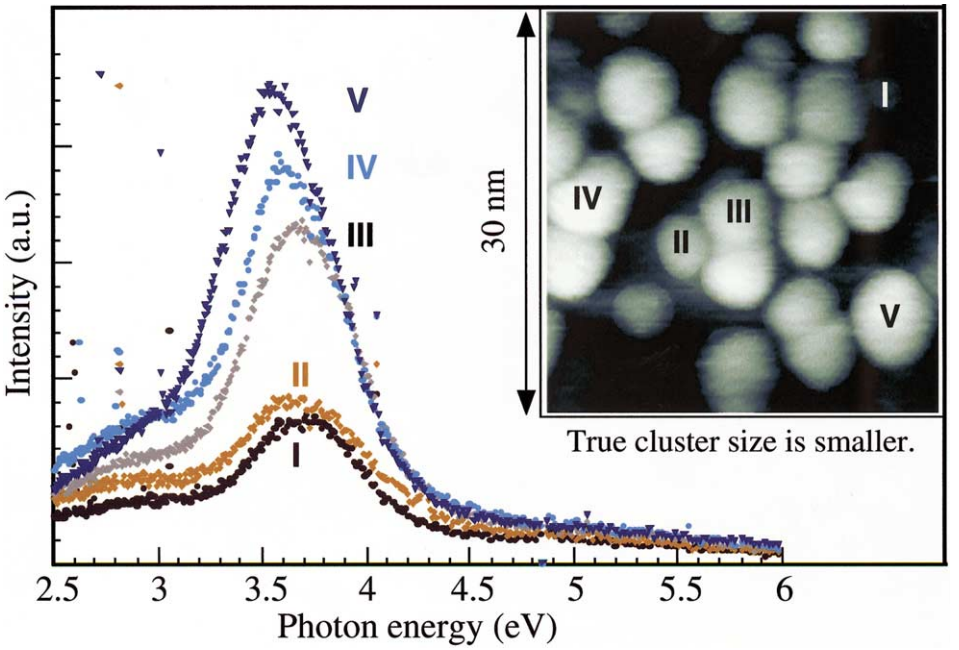

Fig. 11. Photon emission spectra of individual, differently sized Ag-clusters (accumulation time 500 s, $U_{tip} = -10$ V, $I_{gap} = 10$ nA). Though width of emission lines are experimentally broadened, blue-shifts of peaks (to higher energies) are discernable as sizes of probed cluster decrease. True sizes of clusters, displayed in STM image, are significantly smaller, because of tip-convolution effect.

our present result (150 meV for clusters of 10 nm) shows the effect of inhomogeneous line-broadening.

3.2.3. Peak position of Mie-plasmon: dependence on cluster size

The dependence of the resonance position on cluster diameter, determined in the size regime between 1.5 and 12 nm, is shown in Fig. 12(b). At this point, we have to emphasize once more that only the (1,0) mode of the Mie-resonance oscillating perpendicular to the surface plane is accessible to the experiment. The shift of the peak position to higher energies with decreasing cluster sizes is clearly visible in the diagram. This observation is in contrast to extinction cross-section measurements performed on an ensemble of Ag-clusters deposited on quartz-glass [22]. Here, a distinct red-shift of the (1,0) mode with decreasing cluster size had been observed. The result was interpreted as a consequence of a shape transition with cluster size (from oblate to spherical shapes for decreasing cluster diameter). This increase of the axial ratio (cluster height/cluster diameter) is, for electrodynamical reasons, connected with a red-shift of the (1,0) mode and a blue-shift of the (1,1) mode. In the present experiments, a shape dependence of the resonance position can essentially be ruled out. A careful determination of the cluster shapes from STM images leads to an almost constant axial ratio of (0.59 ± 0.10) in the examined size range. Only

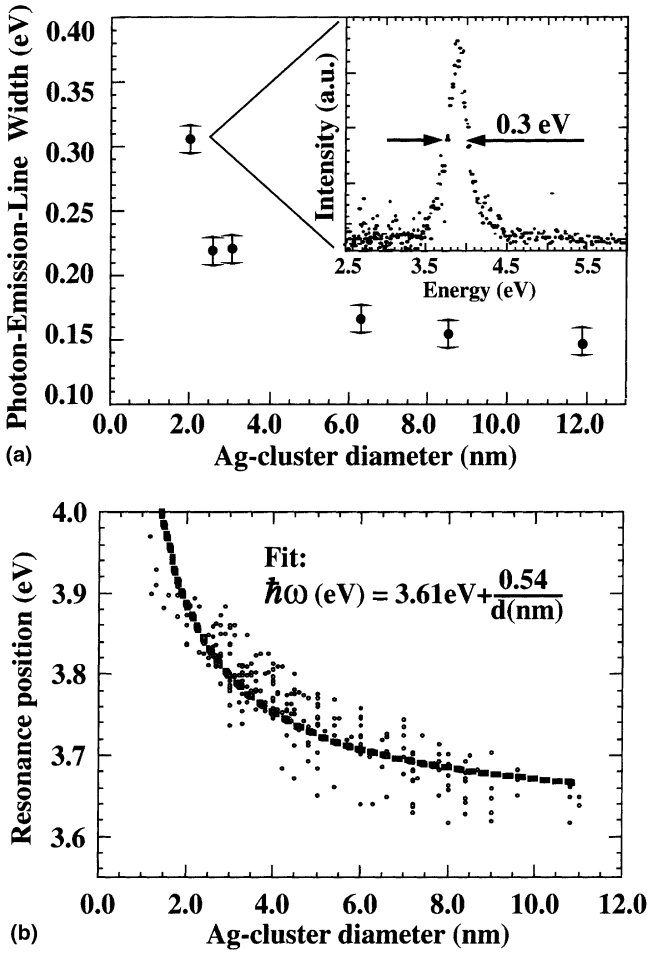

Fig. 12. FWHM and peak positions for light emission from individual Ag-clusters supported on thin alumina film: (a) Inset shows photon emission spectrum measured with high spectral resolution. (b) Dashed curve is fit to measured size dependence (d = diameter) reflecting growing surface contribution to plasmon resonance in small clusters.

particles in the upper size regime generally grow in a more oblate shape with an axial ratio slightly below 0.5.

Neglecting the shape dependence of the resonance position, we concentrate in the following discussion on intrinsic size-effects, as reason for the observed blue-shift of the Mie-resonance. Intrinsic size-effects (e.g., reduction of electron mean free path, hybridization of silver s and d-electrons, spill out of electrons) have a general trend to follow a d^{-1} law (d – cluster diameter) reflecting the growing surface contribution with respect to bulk effects for small particles [21,46]. A corresponding fit function of

the type:

$$\hbar\omega(\mathrm{d}) = \hbar\omega(\infty) + ad^{-1} \tag{3.6}$$

already reveals a qualitative agreement with the experimental data (dashed line in Fig. 12(b)). This d^{-1} behavior further supports our interpretation of the observed blue-shift as a consequence of intrinsic size effects on the Mie-resonance. The above-mentioned contributions to the size-effect cannot be extracted from the experimental data. However, two results of the empirical description have to be emphasized. The value $\hbar\omega(\infty)$ for large Ag-particles should be in agreement with the predictions of the classical Mie-theory. A crude estimation of the resonance position can be derived from the following formula [47]

$$\varepsilon_1(\omega) = -\varepsilon_\mathrm{m}(1 - L_\perp)L_\perp^{-1}, \tag{3.7}$$

where ε_m is the averaged static dielectric constant of the medium surrounding the cluster, consisting of 70% vacuum ($\varepsilon_\mathrm{m} = 1$) and 30% alumina film ($\varepsilon_\mathrm{m} = 3.13$ [48]) and $L_\perp$ is the geometrical depolarization factor along the surface normal estimated at 0.4 for the given cluster shape. Values for the dielectric function of Ag were taken from the literature [49]. The calculated resonance position of 3.45 eV is significantly lower than the experimental value of 3.6 eV. Two reasons may be responsible for this difference. The Ag-clusters are separated from the NiAl-substrate by an alumina film of only 0.5 nm thickness. Therefore, a strong electromagnetic coupling between the oscillating dipole in the cluster and its image dipole in the metal can be expected. This should lead to a reduced polarizability of the cluster and a blue-shift of the resonance position of the oscillation. Additionally, the internal plasmon potential is effected by the electrostatic field induced by the negatively charged tunnel tip. This additional field pushes the Ag-electrons at the exposed surface into the cluster volume and leads to a local increase of the electron density [50]. The result is a further shift of the resonance position to higher energies. However, cathode luminescence measurements performed on a cluster ensemble of $Ag/Al_2O_3/NiAl(1\,1\,0)$, in the absence of an electric field, reveal almost the same value for $\hbar\omega(\infty)$ [51]. A significant field-induced effect on the Mie-resonance position can therefore be excluded.

The factor 'a' describing the size dependence of the resonance position was obtained as 0.54 eV nm from (3.6). For Ag-clusters embedded in weakly interacting media or vacuum, this value is the result of two major, competing processes [52,53]. A decrease of the cluster diameter leads to a growing fraction of electrons residing outside the classical cluster volume. This *spill-out* effect reduces the density of the 5s electrons inside the cluster and lowers the plasma frequency of the electron gas. The spill-out contribution causes a red-shift of the Mie-resonance in small clusters and a negative 'a' value. The size dependent screening efficiency of the Mie-plasmon, due to the Ag 4d-electrons, leads to an opposite size-effect in the resonance energy. The strong depolarization field of the d-bands considerably lowers the plasma frequency of the free-electron gas. The screening efficiency is reduced at the cluster surface, because the d-electrons are stronger localized and cannot spill-out into the vacuum very far. The electron gas at the cluster surface is hardly affected by the depolarization field of the 4d-electrons and enhances its plasma frequency towards the

unscreened value. The growing surface to volume ratio leads to an increase of the total Mie-plasmon energy in small Ag-clusters and counteracts the spill-out effect (high '*a*' value). Our experimentally determined blue-shift of the resonance position for supported Ag-clusters ($a = 0.54$ eV nm) is considerably higher than for Ag-clusters in vacuum ($a = 0.18$ eV nm) [54]. This result seems to be reasonable, because the efficiency of the spill-out effect is strongly reduced at the cluster–alumina interface and its contribution to the frequency-shift should be less important compared to free particles. However, for Ag-clusters enclosed in an argon-matrix the spill-out effect is suppressed at the whole cluster surface [55]. The hybridization effect dominates the size dependence of the Mie-resonance position, thus explaining the pronounced blue-shift. As expected, the corresponding '*a*' factor of 0.8 eV nm, for this system [25], clearly exceeds the value for the supported Ag-clusters, in the present experiment. These considerations give only qualitative arguments for an understanding of the observed dependence of the Mie-resonance on the cluster size. A comprehensive explanation of the observed blue-shift has to include a separate treatment of all the competing processes contributing to the intrinsic size effect, especially the screening efficiency of the Ag 4d-electrons and the electron density variation at the cluster surface and the cluster–oxide interface.

4. Conclusions

During FIM studies, it turns out that lowering the specimen temperature to 35 K improves the image conditions for individual Pt-adatoms, in particular for those deposited on a thin alumina film prepared on a (1 1 0) apex plane of a NiAl-tip. Employing the probe-hole FEM technique, conditions for the preparation of a stoichiometric (Ni 50%, Al 50%) (1 1 0) surface were examined by making use of the sensitivity of the work-function to the surface concentration. It appears desirable to further characterize the binding sites of a Pt-adatom deposited on a NiAl(1 1 0) plane prior to oxidation, in order to produce a precise local length scale. From our present observations, we conclude that the mobility of Pt on NiAl(1 1 0) is significantly *lower* than on Al_2O_3/NiAl(1 1 0). In the latter case, the relatively high mobility at temperatures approaching 100 K is in general agreement with previous STM investigations on Pt–cluster formation, occurring at low temperatures [6]. It is still clear, however, that the characterization of the surface diffusion behavior of alumina-supported platinum requires more displacement observations.

Benefiting from the high lateral resolution of the STM, we were able to perform photon emission spectroscopy on individual, oxide-supported silver clusters. The spectra are dominated by an intense emission line centered around 3.7 eV, which can be attributed to the (1,0) mode of the Mie-resonance in small silver particles. Peak position, FWHM and intensity of the emission line could be determined for a single cluster. The observed blue-shift of the resonance position with decreasing cluster size cannot be explained by a shape transition, but reflects the growing importance of quantum-size effects in the size range examined. The interplay between the electron spill-out and the s-d electron hybridization effect in small Ag-particles is discussed

as a model to understand the observed size dependence of the Mie-plasmon. The importance of cluster–cluster and cluster–substrate interactions for the plasmon oscillation has still to be investigated in more detail. The mutual influence of the electromagnetic fields in neighboring particles causes a shift of the Mie-plasmon to lower energies, which should be detectable as a function of the particle distance. If the thickness of the alumina spacer would be gradually increased, the electromagnetic coupling between the clusters and the underlying NiAl-substrate could be adjusted in a controlled manner. This should also change the resonance position of the Mie-plasmon and could be used to estimate the screening properties of the alumina film. Additionally, the thin oxide film supporting the silver clusters could be replaced by a weakly doped bulk oxide, which would enable the cluster-support interaction to be minimized and the intrinsic position of the Mie-plasmon in silver particles to be determined.

Acknowledgements

For financial support, we are grateful to the Deutsche Forschungsgemeinschaft, the Fond der Chemischen Industrie and the NEDO International Joint Research Grant on Photon and Electron Controlled Surface Processes.

References

[1] C.T. Campbell, Surf. Sci. Rep. 27 (1997) 3.
[2] H.-J. Freund, Angew. Chem. Int. Ed. 36 (1997) 452.
[3] C.R. Henry, Surf. Sci. Rep. 31 (1998) 235.
[4] M. Valden, X. Lai, D.W. Goodman, Science 281 (1998) 1647.
[5] U. Heiz, A. Sanchez, S. Abbet, W.-D. Schneider, J. Am. Chem. Soc. 121 (1999) 3214.
[6] M. Bäumer, H.-J. Freund, Prog. Surf. Sci. 61 (1999) 127.
[7] K. Müller, H. Lindner, D.M. Zehner, G. Ownby, Verhandlungen der Deutschen Physikalischen Gesellschaft 25 (1990) 1130.
[8] G.L. Kellogg, Surf. Sci. 257 (1991) 1.
[9] J. Sotola, Z. Knor, J. Catal. 145 (1994) 501.
[10] D.G. Ren, Surf. Rev. Lett. 2 (1995) 177.
[11] N. Ernst, B. Duncombe, G. Bozdech, M. Naschitzki, H.-J. Freund, Ultramicroscopy 79 (1999) 231.
[12] A. Bettac, L. Köller, V. Rank, K.H. Meiwes-Broer, Surf. Sci. 402 (1998) 475.
[13] J. Li, W.D. Schneider, R. Berndt, S. Crampin, Phys. Rev. Lett. 80 (1998) 3332.
[14] B.C. Stipe, M. Rezaei, W. Ho, Science 280 (1998) 1732.
[15] J.H. Coombs, J.K. Gimzewski, B. Reihl, J.K. Sass, R.R. Schlittler, J. Microscopy 152 (1988) 325.
[16] R. Berndt, Photon emission from the scanning tunneling microscope, in: R. Wiesendanger (Ed.), Scanning Probe Microscopy, in: R. Wiesendanger. K. von Klitzing (Eds.), Springer Series Nanoscience and Technology, Springer, Berlin, 1998 (Chapter 5).
[17] S.F. Alvarado, Ph. Renaud, L. Abraham, Ch. Schönenberger, D.J. Arent, H.P. Meier, J. Vac. Sci. Technol. B 9 (1991) 409.
[18] A. Downes, M.E. Welland, Phys. Rev. Lett. 81 (1998) 1857.
[19] P. Dumas, C. Syrykh, I. Makarenko, F. Salvan, Europhys. Lett. 40 (1997) 447.
[20] R. Berndt, R. Gaisch, J.K. Gimzewski, B. Reihl, R. Schlittler, W.D. Schneider, M. Tschudy, Science 262 (1993) 1425.

[21] U. Kreibig, W. Vollmer, Optical properties of metal clusters, in: U. Gonser, R.M. Osgood, Jr., M.B. Panish, H. Sakai (Eds.), Springer Series Materials Science, in: J.P. Toennies (Ed.) vol. 25, Springer, Berlin, 1995.
[22] T. Wenzel, J. Bosbach, F. Stietz, F. Träger, Surf. Sci. 412 (1999) 257.
[23] D. Martin, J. Jupille, Y. Borensztein, Surf. Sci. 402 (1998) 433.
[24] U. Kreibig, L. Genzel, Surf. Sci. 156 (1985) 678.
[25] W. Ekardt, D. Tran Thoai, F. Frank, W. Schulze, Solid State Commun. 46 (1983) 571.
[26] T. Yamaguchi, S. Yoshida, A. Kinbara, Thin Solid Films 21 (1974) 173.
[27] I. Simonsen, R. Lazzari, J. Jupille, S. Roux, Phys. Rev. B 61 (2000) 7722.
[28] N. Nilius, N. Ernst, H.-J. Freund, Phys. Rev. Lett. 84 (2000) 3994.
[29] M.K. Miller, R. Jayaram, Surf. Sci. 266 (1992) 458.
[30] J. Unger, Yu.A. Vlasov, N. Ernst, Appl. Surf. Sci. 87/88 (1995) 45.
[31] R.M. Jaeger, H. Kuhlenbeck, H.-J. Freund, M. Wuttig, W. Hoffmann, R. Franchy, H. Ibach, Surf. Sci. 259 (1991) 235.
[32] P.L. Cowan, T.T. Tsong, Surf. Sci. 67 (1977) 158.
[33] S.C. Wang, G. Ehrlich, Phys. Rev. Lett. 62 (1989) 2297.
[34] G.L. Kellogg, Surf. Sci. Rep. 21 (1994) 1.
[35] D.A. Reed, G. Ehrlich, J. Chem. Phys. 64 (1976) 4616.
[36] F. Nieto, C. Uebing, Vacuum 54 (1999) 119.
[37] K. Bobev, V. Gaidarova, Phys. Stat. Sol. (a) 23 (1974) K129.
[38] A. Cörper, G. Bozdech, N. Ernst, H.-J. Freund, unpublished.
[39] M.K. Miller, G.D.W. Smith, Atom Probe Microanalysis: Principles and Applications to Materials Problems, Materials Research Society, Pittsburgh, 1989.
[40] Yu. Suchorski, W.A. Schmidt, N. Ernst, J.H. Block, H.J. Kreuzer, Prog. Surf. Sci. 48 (1995) 121.
[41] A. Bogicevic, D.R. Jennison, Phys. Rev. Lett. 82 (1999) 4050.
[42] K. Kyuno, G. Ehrlich, Surf. Sci. 383 (1997) L766.
[43] N. Nilius, N. Ernst, P. Johansson, H.-J. Freund, Phys. Rev. B 61 (2000) 12682.
[44] P. Johansson, R. Monreal, P. Apell, Phys. Rev. B 42 (1990) 9210.
[45] F. Stietz, F. Träger, Philos. Mag. B 79 (1999) 1281.
[46] K.-P. Charlé, L. König, S. Nepijko, I. Rabin, W. Schulze, Cryst. Res. Technol. 33 (1998) 1085.
[47] R. Gans, Ann. Physik 37 (1912) 881.
[48] K.-H. Hellwege, J. Olsen (Eds.), Metals: Electronic Transport Phenomena, Landolt-Börnstein, New Series, Group III, vol.15b, Springer, Berlin, 1985.
[49] H. Ehrenreich, H. Philipp, Phys. Rev. 128 (1962) 1622.
[50] P. Gies, R. Gerhardts, Phys. Rev. B 33 (1986) 982.
[51] M. Adelt, W. Drachsel, H.-J. Freund, unpublished.
[52] W. Ekardt, W.-D. Schöne, J. Pacheco, in: W. Ekardt (Ed.), Metal Clusters, Wiley, New York, 1999, p. 1.
[53] A. Liebsch, Phys. Rev. B 48 (1993) 11317.
[54] J. Tiggesbäumker, L. Köller, K.H. Meiwes-Broer, A. Liebsch, Phys. Rev. A 48 (1998) R1749.
[55] A. Zangwill, in: Physics at Surfaces, Cambridge University Press, Cambridge, 1988, p. 200.